AIAA SciTech Forum
8-12 January 2024, Orlando, FL
AIAA SCITECH 2024 Forum

10.2514/6.2024-2516

Wall-Modeled Large-Eddy Simulation of Supersonic Mixing Layer for Aero-Optical Distortion Analysis

Pedro Castillo* and Andreas Gross†

New Mexico State University, Las Cruces, NM 88003

Aaron Fassler‡, Sergey Leonov§ and Stanislav Gordeyev¶

University of Notre Dame, Notre Dame, IN 46556

The Mach 2 turbulent boundary flow over an optical window that is recessed into a cavity is being considered. A two-dimensional nozzle at the upstream end of the cavity issues a wall-tangential subsonic jet that provides convective cooling of the optical window. The turbulent approach boundary layer mixes with the cooling jet and causes optical distortions to light beams passing through the optical window. The objective of the research is to investigate the aero-optical distortions arising from density fluctuations of the turbulent mixing layer over the optical window. A wall-modeled large-eddy simulation of the experiment in the SBR-50 Supersonic Wind Tunnel at Notre Dame University was carried out. Concerning the approach boundary layer, a convective velocity profile was matched and the root-mean-square optical path distortion is in agreement with a semi-analytical model by Notre Dame University. The root-mean-square optical path distortion over the optical window is within 13% of the measured value. A proper orthogonal decomposition with a density-based kernel reveals that spanwise coherent density fluctuations are chiefly responsible for the optical distortions.

I. Introduction

Flight vehicles often employ optical sensors for tasks such as target acquisition and tracking or landmark-based navigation. At high flight Mach numbers, aero-thermodynamic heating can result in wall recovery temperatures that exceed the limits of existing aerospace materials and optical windows need to be actively cooled. Active cooling through secondary wall-tangential gas injection is an attractive candidate for achieving this objective. This paper is concerned with a canonical optical window that is recessed into a cavity. At the upstream end, the cavity is defined by a cooling gas nozzle exit; At the downstream end, the cavity is terminated by a compression ramp. The pressure, velocity, and temperature of the cooling film will affect the growth of the shear-layer over the optical window. If the nozzle exit pressure is above ambient, an oblique shockwave will form and the cooling film will expand in the streamwise direction. The freestream/cooling-film velocity ratio has a strong effect on turbulent mixing. Since the pressure is nearly constant across the cooling film, the temperature difference between the freestream and the cooling film is directly related to the magnitude of the density gradients which are responsible for the aero-optical distortions. Large density gradients are also expected when the cooling film gas is dissimilar from the ambient gas. The understanding of the source of the aero-optical distortions and the development of models for predicting their intensity (similar to the Notre Dame model for boundary layer flows by Gordeyev et al.[1]) are the main objectives of this research.

---

[*] Graduate Research Assistant, Mechanical and Aerospace Engineering Department. AIAA Member.
[†] Associate Professor, Mechanical and Aerospace Engineering Department. AIAA Associate Fellow.
[‡] Graduate Research Assistant, Aerospace and Mechanical Engineering Department. AIAA Member.
[§] Research Professor, Aerospace and Mechanical Engineering Department. AIAA Associate Fellow.
[¶] Associate Professor, Aerospace and Mechanical Engineering Department. AIAA Associate Fellow.

Copyright © 2024 by the authors. Published by the American Institute of Aeronautics and Astronautics, Inc., with permission.

When collimated light is propagated through compressible boundary and shear layers, aero-optical effects such as image blurring, beam jitter, and offsetting occur. Numerous experimental and numerical investigations have been carried out in order to understand the unsteady flow physics of mixing layers associated with film cooling applications.[2–10] The density fluctuations associated with supersonic turbulent shear layer flows over optical window cavities are the primary cause for optical aberrations.[11, 12] Experiments by Chew[13] revealed that the aero-optical distortions are minimal prior to laminar-turbulent transition, increase rapidly during transition, and remain nearly constant over the fully turbulent regime. According to Zilberter,[14] wavefront distortions are driven by shear-layer oscillations at the Rossiter frequencies. Fox[15] found that the passage of large-scale structures through the beam path has the strongest effect on the statistics of the optical beam deflection. Ayyalasomayajula et al.[16] proposed that wavefront phase aberrations and root-mean-square optical path differences (OPD_{rms}) mainly result from shocklets downstream from the cooling film injection.

A multi-tiered approach of experiments and theory at Notre Dame University (ND) as well as wall-modeled large-eddy simulations (WMLES) at New Mexico State University (NMSU) is taken to understand and model the aero-optics of turbulent supersonic boundary layer flows over optical windows with film cooling. The experiments are carried out in the SBR-50 Supersonic Wind Tunnel[17] at ND. The WMLES at NMSU model the ND experiment. The freestream Mach number is $M_\infty = 2.0$ and the momentum-thickness Reynolds number for the approach boundary layer is $Re_\theta = 21,750$. First, the numerical method and computational grid are introduced. Then, the approach boundary layer is characterized. The flow over the cavity is discussed next. The OPD_{rms} for the cavity is compared with the experiment and a proper orthogonal decomposition of the density fluctuations is carried out to determine the leading contributor to the optical distortions.

II. Methodology

A. Numerical Method

The compressible Navier-Stokes equations in the finite volume formulation were solved with an in-house developed research code.[18, 19] The convective fluxes were computed with the Lax-Friedrichs (maximum eigenvalue over stencil width) scheme and interpolated onto the cell faces with a ninth-order-accurate weighted essentially non-oscillatory scheme.[20] A fourth-order-accurate discretization was employed for the viscous terms. The governing equations were integrated in time with the second-order-accurate implicit trapezoidal rule. The perfect gas state equation was used to model the gas behavior. The dynamic viscosity was obtained from Sutherland's law.

B. Reference Parameters and Non-Dimensionalization

The freestream Mach number for the SBR-50 Supersonic Wind Tunnel experiments at ND is $M_\infty = 2.0$. The operating gas is air. The stagnation pressure is $p_0^* = 2.6 \times 10^5 Pa$ and the stagnation temperature is $T_0^* = 300K$. Here, the asterisk indicates dimensional quantities. Approach boundary layer profiles were obtained from double Fourier transforms of time-resolved Schlieren visualizations. The boundary layer thickness and momentum thickness are approximately $\delta^* = 3.2mm$ and $\theta^* = 0.275mm$.

For the simulations, all length scales were made dimensionless with an arbitrary reference length, $L_{ref}^* = 1m$. The freestream velocity was taken as reference velocity, u_∞^*. Density was made dimensionless by the freestream density, ρ_∞^*. The temperature and pressure were made dimensionless with the freestream temperature, T_∞^*, and two times the freestream dynamic pressure, $\rho_\infty^* u_\infty^{*2}$, respectively. Time was normalized by L_{ref}^*/u_∞^*. Viscosity was made dimensionless with $\mu_\infty^* = 1.1325 \times 10^{-4} kg/(ms)$. The Reynolds number based on the reference quantities is $Re = 31.73 \times 10^6$. The laminar and turbulent Prandtl number are $Pr = 0.71$ and $Pr_T = 0.9$, respectively. The momentum thickness Reynolds number is $Re_\theta = 9,190$.

The cooling film is injected with a converging two-dimensional nozzle that issues a wall-tangential jet over the optical window. The nozzle inflow and outflow duct height are $50.8mm$ and $4mm$, respectively. In the ND experiments, flow straighteners inside the nozzle condition the flow. The flow straighteners were not resolved in the simulation. Instead, below $y = -0.025$ (see Fig. 1) the x-velocity (u) was forced to zero via an x-momentum equation right-hand-side forcing term,

$$\frac{\partial(\rho u)}{\partial t} + \nabla \cdot (\rho u \mathbf{u}) = -\nabla p + \nabla \cdot \boldsymbol{\tau} - 100\rho u\,. \tag{1}$$

This not only straightened out the flow but also suppressed flow separation near the top-left corner of the nozzle. Assuming a constant total enthalpy and isentropic flow, the nozzle inflow and outflow Mach number are related via,

$$\frac{A_{in}}{A_{out}} = 12.7 = \frac{M_{out}}{M_{in}} \left[\left(1 + \frac{\gamma - 1}{2} M_{in}^2 \right) / \left(1 + \frac{\gamma - 1}{2} M_{out}^2 \right) \right]^{\frac{\gamma+1}{2(\gamma-1)}} . \tag{2}$$

For an outflow Mach number of $M_{out} = 0.533$, the inflow Mach number is $M_{in} = 0.0356$. The static pressure at the nozzle exit was matched to the freestream pressure, $p^*_{exit} = p^*_\infty = 33,229 Pa$. From this, the nozzle total pressure is obtained,

$$p^*_0 = p^*_{out} \left(1 + \frac{\gamma - 1}{2} M_{out}^2 \right)^{\frac{\gamma}{\gamma-1}} = 40,319 Pa \, . \tag{3}$$

The jet flow stagnation temperature is 300K. The freestream (primary stream) and nozzle (secondary stream) exit Mach number, total pressure and total temperature, as well as freestream and nozzle exit velocity and temperature are provided in Tab. 1.

Table 1. Flow properties.

Flow properties	Primary stream	Secondary stream
M_∞	2.0	0.533
$p^*_o(Pa)$	2.6×10^5	40,319
$T^*_o(K)$	300	300
$u^*_\infty(m/s)$	517.75	184.03
$T^*_\infty(m/s)$	166.7	283.9

The computational time-step for the simulation was $\Delta t = 0.0005$. The simulation was advanced in time over a time-interval of 9 after which the flow was stationary. A time average and statistical quantities were then computed over a time interval of 5 and averaged in the homogeneous spanwise direction.

C. Boundary Conditions

No-slip and no-penetration conditions were enforced at the walls, which were treated as adiabatic. Dirichlet conditions were applied at the inflow and freestream boundary, and Neumann conditions were employed at the outflow boundary. Flow periodicity was enforced in the spanwise direction. The rescaling and recycling method by Stolz and Adams[21] was employed to sustain a turbulent approach boundary layer flow. The recycling plane was placed at $x = 0.115$. Details about the implementation of the rescaling and reycling method can be found in Gross et al.[22]

D. Wall-Modeling

For high-Reynolds number turbulent wall-bounded flows, the near-wall grid resolution requirement can become prohibitive unless the near-wall turbulence is modeled. Rather then resolving the near-wall region, ordinary differential equations for the streamwise momentum and energy are solved from a matching point to the wall to obtain the wall shear stress and wall temperature. Details about the implementation of the wall model are provided in Castillo et al.[23]

E. Sub-Grid Stress and Heat Flux

The sub-grid stress (SGS) tensor, $\bar{\rho}\tau_{ij} = \bar{\rho}\overline{u'_i}\,\overline{u'_j} - \overline{\rho u'_i u'_j}$, is modeled as

$$\bar{\rho}\tau_{ij} = 2\mu_T \left(S_{ij} - \frac{1}{3} S_{kk} \delta_{ij} \right) - \frac{2}{3} \bar{\rho} k \delta_{ij} \, , \tag{4}$$

with sub-grid eddy-viscosity, μ_T, strain rate tensor, S_{ij}, Kronecker symbol, δ_{ij}, and turbulence kinetic energy, k. The sub-grid heat flux is modeled as

$$q_i = -k_T \frac{\partial T}{\partial x_i} \, , \tag{5}$$

with

$$k_T = k \frac{\mu_T}{\mu} \frac{Pr}{Pr_T} \, . \tag{6}$$

F. Sub-Grid Stress Model

The WALE model by Nicoud and Ducros[24] was employed for computing the sub-grid (unresolved) eddy-viscosity,

$$\mu_T = \bar{\rho}(C_w \Delta)^2 \frac{(S^d_{ij} S^d_{ij})^{3/2}}{(S_{ij} S_{ij})^{5/2} + (S^d_{ij} S^d_{ij})^{5/4}} \, , \tag{7}$$

where

$$S^d_{ij} = \frac{1}{2} \left(g^2_{ij} + g^2_{ji} \right) - \frac{1}{3} \delta_{ij} g^2_{kk} \tag{8}$$

is the trace-less symmetric part of the square of the velocity gradient tensor and $g^2_{ij} = g_{ik} g_{kj}$. For the present results, the model constant, C_w, was taken as 0.325. The grid length-scale, Δ, was taken as the geometric average of the cell dimensions. The isentropic unresolved TKE was computed as

$$k = \frac{1}{2} \tau_{kk} = \left(\frac{\mu_T}{0.094 Re \rho \Delta} \right)^2 \, . \tag{9}$$

G. Computational Grid

Using analytical functions, a body-fitted computational grid was generated for the geometry of the ND experiments (Fig. 1). The grid is divided into three sub-domains or blocks. Information about the blocks is provided in Tab. 2. Block 1 is rectangular and features a constant grid-line spacing in the streamwise direction that is reduced near the outflow to resolve the corner flow. Following suggestions by Larsson et al.,[25] for an estimated boundary layer thickness of $\delta \approx 0.06$, a wall-normal grid line spacing of $\Delta y/\delta = 0.02$ was employed between the wall and $y/\delta = 0.2$. Outside the near-wall region ($y/\delta \leq 0.2$), the wall-normal grid line stretching is initially 5% and then decreases away from the wall. Block 2 is primarily rectangular but features a compression ramp at the outflow. The height of the backward facing step is $h = 0.005$, which is $1mm$ more than the nozzle exit height. This can be explained by the finite thickness of the nozzle lip in the experiment. For the present simulation, the nozzle exit height is assumed to be identical to the step height (zero thickness nozzle lip). Ultimately, this amounts to a truncation of the nozzle. The compression ramp starts at $x = 0.24$ and the ramp angle is $\alpha = 4deg$. Similar to block 1, a layer with constant wall-normal grid distribution is employed at the wall. Inside block 2, the streamwise grid line spacing is constant. At the inflow, grid refinement is employed to resolve the corner flow. The streamwise grid line spacing increases near the outflow to dissipate flow structures. Downstream of the block 2 inflow, the grid lines are redistributed in the wall-normal direction to obtain a more balanced grid line distribution. The block 3 (nozzle) grid was created with a Poisson grid generator.[26] The two-dimensional grids were extruded in the spanwise direction using an equidistant grid line distribution.

Table 2. Domain size and number of cells per block.

Block	Domain size		Number of cells	Total number of cells
1 (Inflow)	$0.130 \times 0.03668 \times 0.0065$	$26h \times 7.33h \times 1.3h$	$512 \times 64 \times 80$	2.62×10^6
2 (Cavity)	$0.173 \times 0.04168 \times 0.0065$	$35.6h \times 8.33h \times 1.3h$	$666 \times 102 \times 80$	5.43×10^6
3 (Nozzle)	$0.0762 \times 0.073 \times 0.0065$	$15h \times 14.6h \times 1.3h$	$192 \times 38 \times 80$	0.58×10^6

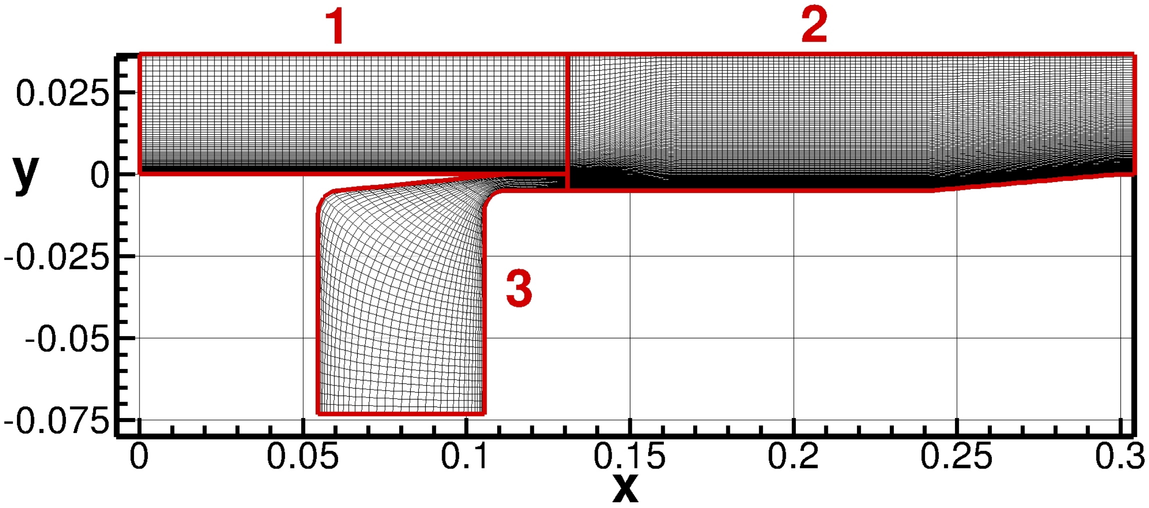

Figure 1. Computational grid. For clarity, every other grid line is omitted for blocks 1 and 2.

H. Optical Path Length and Optical Path Difference

To investigate the optical aberrations, the density fields were first converted into index-of-refraction, n, fields via the linear Gladstone-Dale relation,[27]

$$n = 1 + K_{GD}\rho \, , \tag{10}$$

where $K_{GD} = 2.27 \times 10^4 \, m^3/kg$ is the Gladstone-Dale constant for air over the pressure and temperature range of the present simulation.[28, 29] Wall-normal integration of the index-of-refraction from the wall to the freestream provides the optical path length,

$$OPL(x,z,t) = \int_0^y n(x,y,z,t)\, dy \, . \tag{11}$$

The mean piston, tip, and tilt is then removed to obtain the optical path difference,

$$OPD(x,z,t) = OPL(x,z,t) - (m_x x + m_z z + b) \, . \tag{12}$$

The coefficients for the correction are found from a least-squares fit over an aperture,

$$R = \int_x \int_z \left[OPL(x,z,t) - (m_x x + m_z z + b)\right]^2 dxdz \, . \tag{13}$$

Aperture in this context refers to the x and z range over which the OPD is computed. The minimization of Eqn. 13 provides a system of equations that is solved for the unknowns m_x, m_z and b. In the study of aero-optical properties of turbulent boundary layers, the root-mean-square of the OPD is often considered,

$$OPD_{rms} = \sqrt{\langle OPD^2(x,z,t)\rangle} \, . \tag{14}$$

In this paper, the OPD_{rms} obtained from the present simulations is compared with a relationship proposed by Gordeyev et al.[1] (Notre Dame model),

$$f\left(M_\infty\right) = \frac{OPD_{rms}}{K_{GD}\rho_\infty c_f^{0.5} M_\infty^2 \delta} \, , \tag{15}$$

where c_f is the skin-friction coefficient and δ is the boundary layer thickness.

I. Proper Orthogonal Decomposition

The proper orthogonal decomposition (POD) by Lumley[30] is a useful tool for the analysis of turbulent flows. Typically, the computationally efficient "snapshot" method by Sirovich[30] is employed. The POD is optimal in the sense that it provides the most compact representation (least number of modes required) of unsteady flows. For incompressible flows, the POD kernel is based on twice the kinetic energy,

$$u_i u_j \,. \tag{16}$$

The Mach 2 case considered here is compressible and the interest is in the density fluctuations because they cause the optical distortions. Therefore, a density-based kernel was considered as well,

$$\rho_i \rho_j \,. \tag{17}$$

The POD modes are orthogonal and sorted according to their respective eigenvalue magnitude. The eigenvalue magnitude is identical to the root-mean-square (rms) velocity (kernel 1) or density (kernel 2) fluctuations. The instantaneous density can be reconstructed from the time-coefficients, $a_i(t)$, and POD modes, $q_i(\mathbf{x})$, via

$$\rho(\mathbf{x}, t) = \sum_i a_i(t) q_i(\mathbf{x}) \,. \tag{18}$$

III. Results

The approach boundary layer flow is discussed first. The compressible displacement thickness, δ^*, momentum thickness, θ, and incompressible shape factor, H_i, are plotted in Fig. 2a. The incompressible shape factor is about 1.26 and slightly below the typical range for turbulent boundary layers ($1.3 \leq H_i \leq 1.4$). In Fig. 2b, the van Driest transformed velocity,

$$u^{VD} = \int \sqrt{\frac{\rho}{\rho_w}} du^+ \,, \tag{19}$$

is plotted versus the wall distance in wall units, y^+. The solid line of the profile indicates the resolved part of the flow and the dashed line signifies the modeled part. The wall model matching point is at $y^+ \approx 175$. For comparison, relationships for the viscous sublayer, $u^+ = y^+$, and the log-layer, $u^+ = 5 + (\ln y^+)/0.41$, (dotted and dashed black lines) are included. The log-layer slope is matched with good accuracy and the defect layer is well represented.

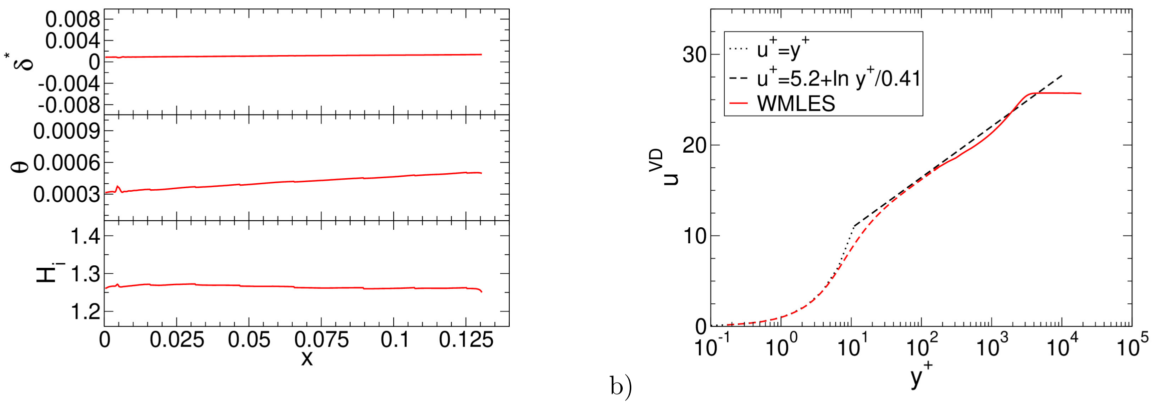

Figure 2. a) Compressible displacement and momentum thickness, and incompressible shape factor. b) Velocity profile in wall units (·····, viscous sublayer relationship, - - -, log-layer relationship, - - -, from wall model, ——, resolved).

Profiles of the streamise velocity, temperature and rms velocity fluctuations were extracted at $x = 0.12$. Velocity and temperature profiles are plotted in Fig. 3. For comparison, profiles from a wall-resolved LES by Lee and Gross[31] of a $M_\infty = 2.05$ turbulent boundary layer at a roughly ten times smaller momentum thickness Reynolds number are included (black lines). As before, the dashed lines represent the modeled part of the profiles and the solid lines indicate the resolved part of the profiles. The wall temperature is about the same for both simulations. For the WMLES, the near-wall temperature gradient is steeper as a result of the higher Reynolds number. The rms velocity fluctuations in the streamwise, wall-normal, and spanwise direction, normalized by the freestream velocity, are compared in Fig. 4. The dashed orange lines indicate the wall model matching point. Good qualitative agreement is observed between the profiles from the present WMLES and the earlier wall-resolved LES by Lee and Gross.[31]

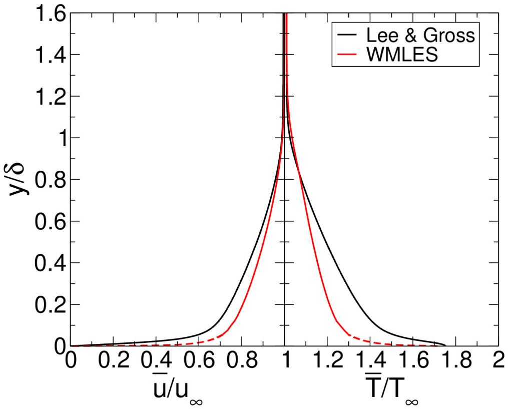

Figure 3. Mean velocity and temperature profiles plotted against wall distance (- - -, from wall model, —, resolved).

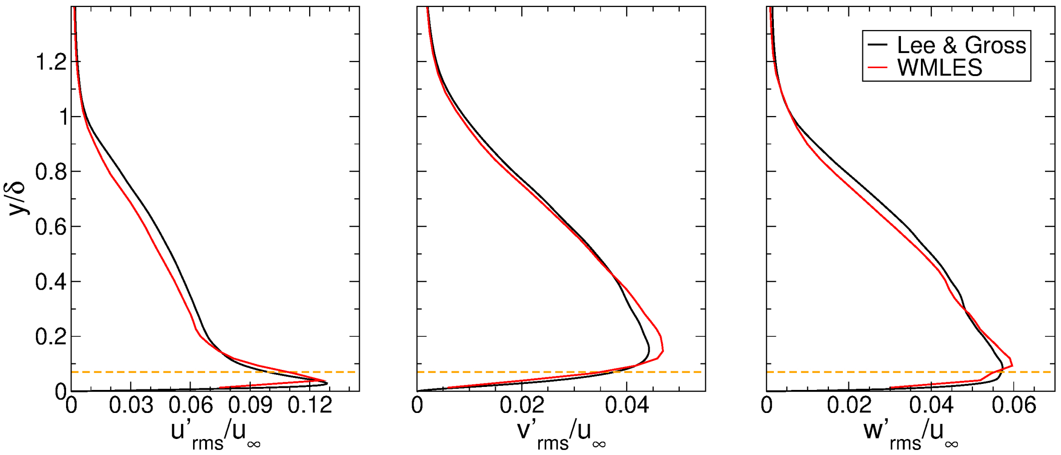

Figure 4. Profiles of resolved root-mean-square velocity fluctuations.

The approach boundary layer flow (block 1) was passed into the cavity domain (block 2). Iso-contours of the mean Mach number and static temperature (in Kelvin) are shown in Fig. 5. In the figure, all distances are normalized by the step height, h, and the x-coordinate is shifted such that the nozzle exit is at $x = 0$. For the selected total temperature ratio, the jet flow is hotter than the freestream. Downstream of the nozzle exit, the boundary layer and cooling film form a shear layer and mix. The temperature contours indicate that around $x/h \approx 10$ the mean shear layer reaches the bottom of the cavity.

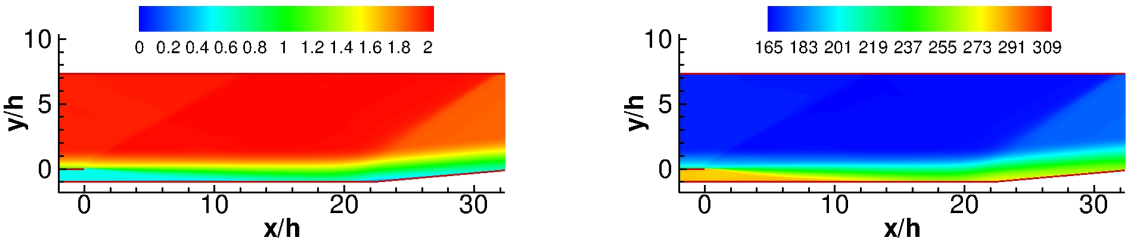

a) b)

Figure 5. a) Mach number and b) static temperature (in Kelvin) at the cavity.

Iso-contours of the density gradient magnitude ("numerical schlieren" image) are shown in Fig. 6a. The turbulent boundary layer spreads quickly after separation and reattaches around $x = 0.18$. The compression ramp deflects the boundary layer upward, leading to a weak compression wave.

In the ND experiment, the convection speed was computed from the optical distortions for the box outlined in Fig. 6a which has dimensions of $28 \times 20 mm$. When double Fourier transforms of the aero-optical distortions are taken, the convection speed manifests itself as a diagonal branch in the spectrum.[32] The slope of the branch is equal to the convective speed, $u_c = \partial\omega/\partial\alpha$, where ω and α are the angular frequency and streamwise wavenumber. Due to aliasing, additional branches appear. To extent the frequency range of the main branch and improve the accuracy of the convective speed estimate, the spectrum is repeated in both α and ω. This approach is known as stacking method.[33,34]

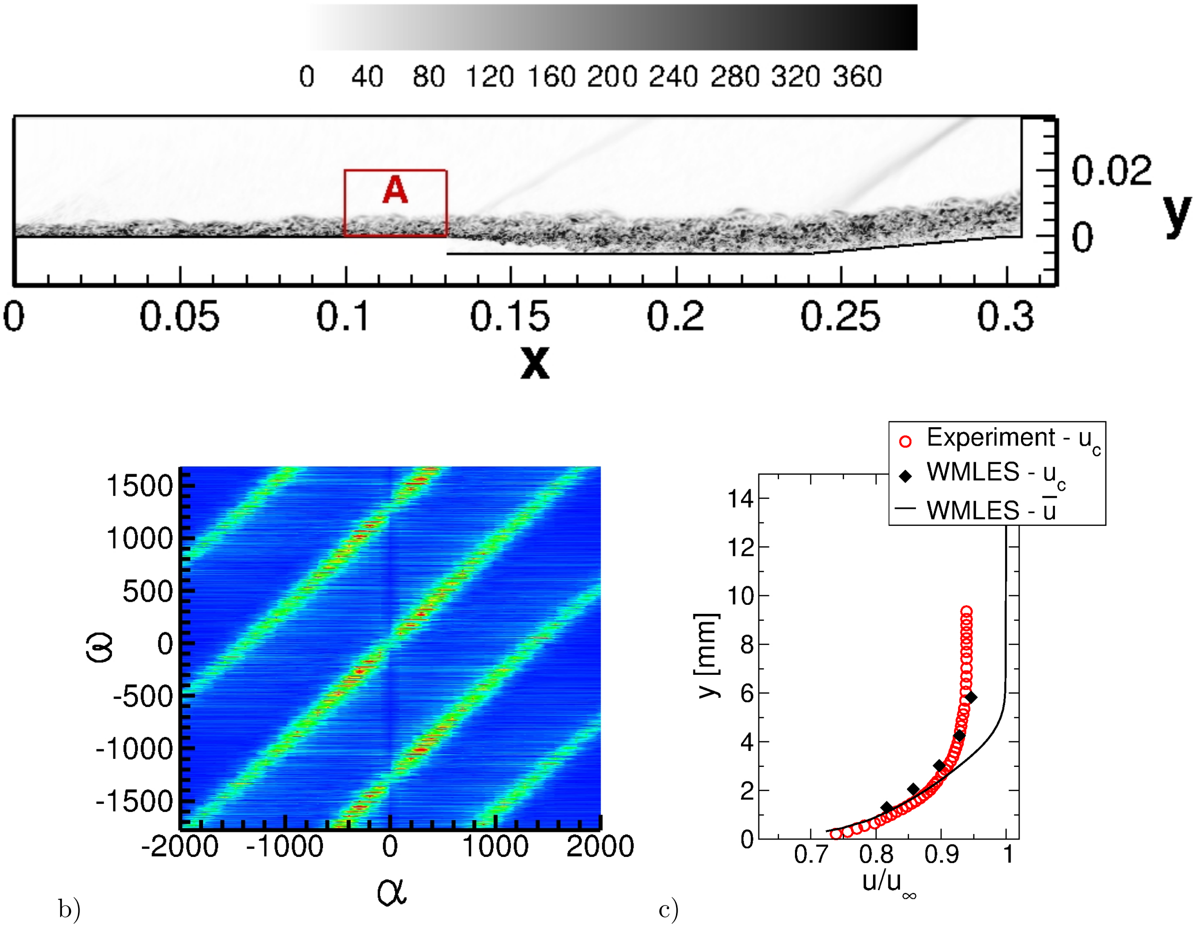

a)

b) c)

Figure 6. a) Iso-contours of density gradient magnitude. b) Spatio-temporal Fourier transform for box A. c) Velocity profiles for box A.

Different from the experiment, the density fluctuations (and not the optical distortions) were Fourier transformed in time and space. A total of 500 density fields were analyzed. The density fields were saved at time intervals of 0.0025. A spectrum for box A (incoming boundary layer) at $(y, z) = (0.00582, 0.00325)$ is shown in Fig. 6b. The slope of the main branch gives the convection velocity, u_c. This procedure was repeated for five different wall-normal locations. In Fig. 6c, the computed convective speeds are compared with a convection velocity profile measured by Fassler et al.[32] The u_c-profile obtained from the simulation is slightly thicker than the measured u_c-profile. The mean $\overline{u}$-velocity profile from Fig. 3 is included for comparison. The convection velocity at the boundary layer edge is approximately 95% of the freestream velocity.

IV. Aero-Optical Characterization

The optical path distortion (OPD) for the approach boundary layer was computed from 1000 density fields that were saved at time intervals of 0.0025. An aperture with streamwise and spanwise extent of $Ap_x \times Ap_z \approx 6\delta \times 1.1\delta \approx 5.5h \times 1.3h$ was analyzed. For the analysis, the beam incidence angle was assumed to be normal to the bottom wall. In Fig. 7, the normalized OPD, $f(M_\infty)$ from Eq. 15, is plotted against the ND model relationship.[35,36] The OPD obtained from the present WMLES is $f(M_\infty) = 0.1458$, and within 2% of the model prediction for $M_\infty = 2$.

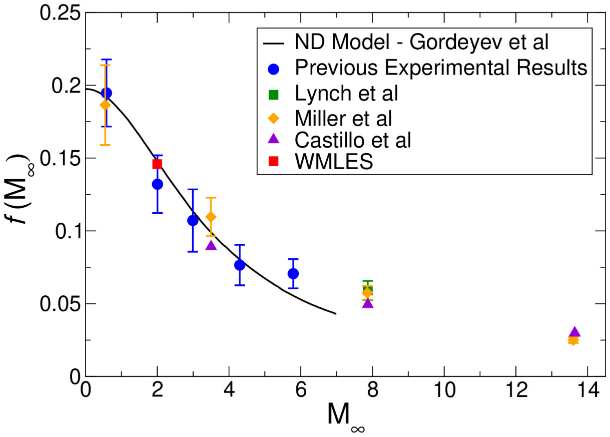

Figure 7. Normalized OPD_{rms}. Notre Dame model,[35,36] previously published numerical[37,38] and experimental data.[34]

The optical path distortion was also computed for an aperture inside the cavity that stretches from $12.7mm$ to $63.5mm$ downstream of the nozzle exit. In Fig. 8, iso-surfaces of the Q-criterion by Hunt[39] are plotted for the approach boundary layer and the cavity. The thick white lines represent the direction of the beam (in the wall-normal direction) and the streamwise extent of the aperture is indicated.

An instantaneous OPL distribution over the cavity is provided in Fig. 9a. The temperature mismatch between the incoming boundary layer and the cooling flow results in a strong two-dimensional density adjustment at the onset of the shear layer which leads to a steady OPD that far outweighs the unsteady OPD. The instantaneous OPD was obtained by subtracting the mean OPL from the instantaneous OPL. An instantaneous OPD corrected for piston, tip, and tilt is shown in Fig. 9b. The OPD fluctuations appear random, as would be expected for a turbulent shear layer. The OPD_{rms} for the cavity aperture is $0.03804\mu m$ and in good agreement with the ND experiment, which reported a range of values between 0.029 and $0.047\mu m$, with a mean value of $0.038\mu m$.[40]

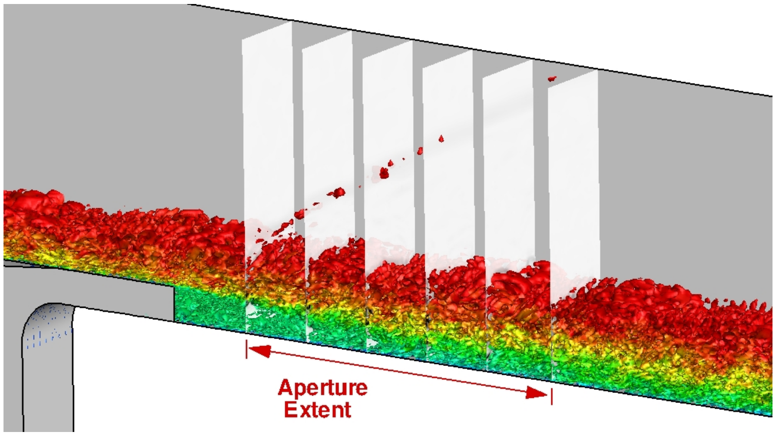

Figure 8. Instantaneous iso-surfaces of $Q = 10$ flooded by streamwise velocity.

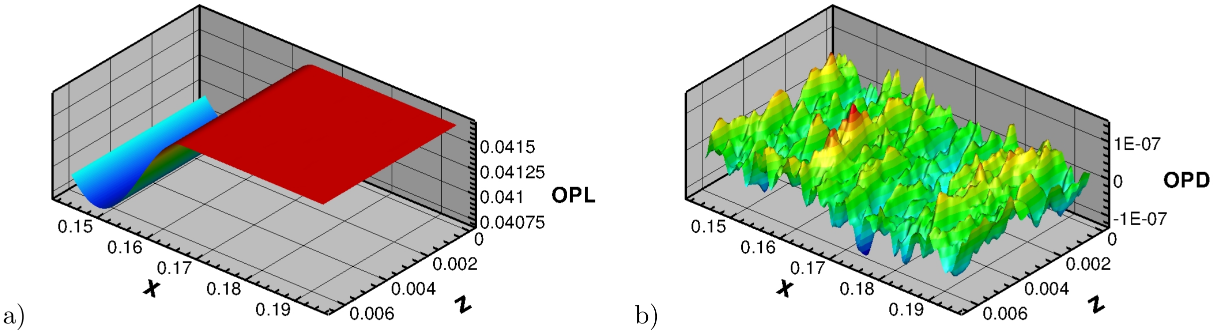

Figure 9. Instantaneous a) OPL and b) OPD for cavity aperture at same time instant.

A. Proper Orthogonal Decomposition

The upstream part of the shear layer was analyzed with the POD. A total of 500 snapshots saved at time intervals of 0.0025 were considered. The POD eigenvalues, λ_i, for the two different kernels are provided in Fig. 10a. For the density-based kernel, the first two unsteady modes form a pair and capture traveling waves. In Fig. 10b, the sum of the leading "$i_{unsteady}$" eigenvalues divided by the sum over all eigenvalues,

$$\frac{\sum_{i=1}^{i=i_{unsteady}} \lambda_i}{\sum_{i=1}^{i=i_{max}} \lambda_i}, \tag{20}$$

is plotted for the different kernels. For the density-based kernel, the eigenvalues add up faster.

Visualizations of the leading unsteady POD mode for both kernels are provided in Fig. 11. Iso-surfaces of the Q-criterion flooded by the streamwise velocity for the velocity-based kernel reveal no large-scale coherent structures (Fig. 11a). Density iso-surfaces for the density-based kernel in Fig. 11b exhibit large spanwise coherent structures. Mode 2 for the density-based kernel is similar to mode 1 but phase-shifted in the streamwise direction by a quarter wavelength. The time-coefficients for modes 1 and 2 are also similar and phase shifted. According to Taira et al.,[30] POD modes with similar shapes that are shifted in the advection direction by a quarter wavelength capture traveling waves. The structures are reminiscent of coherent flow structures in turbulent shear layers.[41]

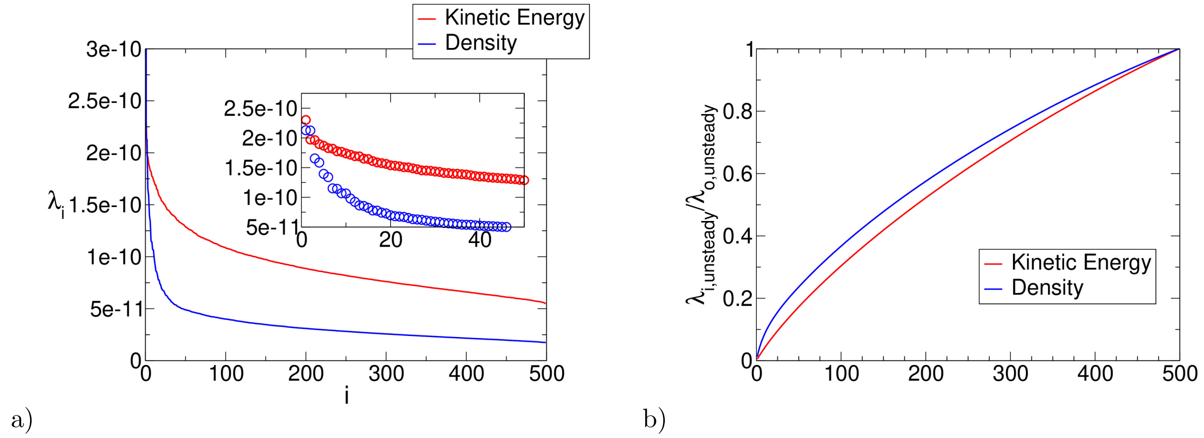

Figure 10. a) Proper orthogonal decomposition eigenvalues (Kernel based on: ——, Kinetic Energy; ——, Density), and b) cumulative energy content of unsteady modes.

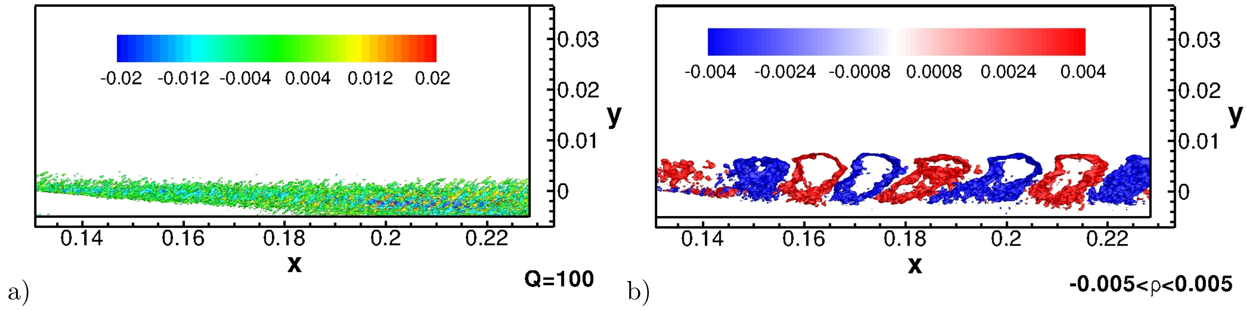

Figure 11. Leading unsteady POD modes for a) kinetic energy-based kernel (iso-surfaces of Q=100 flooded by streamwise velocity) and b) density-based kernel (iso-surfaces of $\rho = \pm 0.005$ flooded by density magnitude).

V. Conclusions

Active cooling can prevent heat damage to optical windows in high-speed flight. Researchers at Notre Dame University (ND) have developed a canonical geometry for investigating the effect of film cooling at supersonic speeds on the optical path difference (OPD). In the ND experiments, a turbulent boundary layer passes over a cavity, with a cooling film issued wall-parallel from the upstream end of the cavity. An optical window is placed at the bottom of the cavity and at the opposite wall to provide aero-optical measurements. A wall-modeled large-eddy simulation (WMLES) of the experiment was carried out for a freestream Mach number of two and a freestream stagnation temperature of 300K. A measured convective velocity profile for the approach boundary layer was matched. Profiles of the root-mean-square (rms) velocity fluctuations obtained from the present WMLES and a wall-resolved LES by Lee and Gross[31] are in adequate agreement.

The optical path length (OPL) was computed by wall-normal integration of the index of refraction. The instantaneous OPD was obtained by subtracting the mean OPL and instantaneous piston, tip, and tilt. The normalized rms OPD for the turbulent approach boundary is in good agreement with a theoretical relationship by Gordeyev et al.[35,36] (i.e., ND model) and previously published experimental and numerical data. Using the same procedure, the rms OPD for the mixing layer was computed and found to be in good agreement with the experimental value.

The turbulent mixing layer flow was also analyzed with the proper orthogonal decomposition (POD). For the chosen sampling interval, with a kinetic energy-based kernel, the POD failed to isolate the dominant large-scale flow structures. With a density-based kernel, large-scale spanwise coherent structures were identified. Future work will focus on making a direct connection between the unsteady flow physics and the observed aero-optical distortions. In addition, different freestream total temperatures will be considered and preparations are made for simulations with dissimilar gases (freestream and cooling flow).

VI. Acknowledgements

This research is funded by the Office of Naval Research (ONR) under grant number N00014-22-1-2454 with Dr. Eric Marineau serving as program manager. High Performance Computing (HPC) resources were provided by the Department of Defense HPC Modernization Program.

References

[1] Gordeyev, S., Jumper, E., and Hayden, T. E., "Aero-Optical Effects on Supersonic Boundary Layers," *AIAA Journal*, Vol. 50, No. 3, 2012.

[2] Juhany, K. and Hunt, M., "Flowfield Measurement in Supersonic Film Cooling Including the Effect of Shock-Wave Interaction," *AIAA Journal*, Vol. 32, No. 3, 1994, pp. 578–585.

[3] Juhany, K., Hunt, M., and Sivo, J., "Influence of Injectant Mach Number and Temperature on Supersonic Film Cooling," *Journal of Thermophysics and Heat Transfer*, Vol. 8, No. 1, 1994, pp. 59–67.

[4] Aupoix, B., Mignosi, A., Viala, S., Bouvier, F., and Gaillard, R., "Experimental and Numerical Study of Supersonic Film Cooling," *AIAA Journal*, Vol. 36, No. 6, 1998, pp. 915–923.

[5] Peng, W. and Jiang, P., "Influence of Shock Waves on Supersonic Film Cooling," *Journal of Spacecraft and Rockets*, Vol. 46, No. 1, 2009, pp. 67–73.

[6] Konopka, M., Meinke, M., , and Schröder, W., "Large-Eddy Simulation of Supersonic Film Cooling at Laminar and Turbulent Injection," *AIAA Paper 2011-2250*, 2011.

[7] Windisch, C., Reinartz, B., and Müller, S., "Numerical Simulation of Coolant Variation in Laminar Supersonic Film Cooling," *AIAA Paper 2012-0949*, 2012.

[8] Dahmen, W., Gotzen, T., Melian, S., , and Müller, S., "Numerical Simulation of Cooling Gas Injection Using Adaptive Multiscale Techniques," *Computers and Fluids*, Vol. 71, 2013, pp. 65–82.

[9] Konopka, M., Meinke, M., and Schröder, W., "Large-Eddy Simulation of Shock-Cooling-Film Interaction at Helium and Hydrogen Injection," *Physics of Fluids*, Vol. 25, No. 10, 2013.

[10] Peng, W. and Jiang, P., "Effect of Shock Waves on Supersonic Film Cooling with a Slotted Wall," *Applied Thermal Engineering*, Vol. 62, No. 1, 2014, pp. 187–196.

[11] Jumper, E. and Fitzgerald, E., "Recent Advances in Aero-optics," *Progress in Aerospace Sciences*, Vol. 37, 2001, pp. 299–339.

[12] Guo, G., Tong, X., and Luo, Q., "Numerical Investigation on Image Degradation Caused by Aero-Optical Effects of the Supersonic Mixing Layer," *Applied Optics*, Vol. 59, No. 35, 2020.

[13] Chew, L. and Christiansen, W., "Experimental Investigation of Transitional Free Shear Layer Optics," *AIAA Journal*, Vol. 31, 1993, pp. 2290–2295.

[14] Zilberter, I., Edwards, J., and Wittich, D., "Numerical Simulation of Aero-Optical Effects in a Supersonic Cavity Flow," *AIAA Journal*, Vol. 55, 2017, pp. 3095–3108.

[15] Fox, T., McKeon, B., and Gordeyev, S., "Effect of Coherent Structures on Aero-Optical Distortion in a Turbulent Boundary Layer," *AIAA Journal*, Vol. 57, 2019, pp. 2828–2839.

[16] Ayyalasomayajula, H., Arunajatesan, S., C., K., and N., S., "Large Eddy Simulation of a Supersonic Flow Over a Backward-Facing Step For Aero-Optic Analysis," *AIAA Paper 2006-1416*, 2006.

[17] Andrews, P., Lax, P., Elliott, S., Firsov, A., and Leonov, S., "Flow Characterization at Heated Air Supersonic Facility SBR-50," *Fluids*, Vol. 7, No. 5, 2022.

[18] Gross, A. and Fasel, H., "High-Order WENO Schemes Based on the Roe Approximate Riemann Solver," *AIAA Paper 2002-2735*, 2002.

[19] Gross, A. and Fasel, H., "High-Order Accurate Numerical Method for Complex Flows," *AIAA Journal*, Vol. 46, No. 1, 2008, pp. 204–214.

[20] Balsara, D., Garain, S., and Shu, C. W., "An Efficient Class of WENO Schemes with Adaptive Order," *Journal of Computational Physics*, Vol. 326, 2016, pp. 780–804.

[21] Stolz, S. and Adams, N., "Large-Eddy Simulation of High-Reynolds-Number Supersonic Boundary Layer using the Approximate Deconvolution Model and a Rescaling and Recycling Technique," *Physics of Fluids*, Vol. 15, No. 8, 2003, pp. 2398–2412.

[22] Gross, A., Castillo, P., and Lee, S., "Wall-Modeled Large-Eddy Simulations of Turbulent Shockwave Boundary Layer Interaction and Boundary Layer Flows," *AIAA Paper 2021-2749*, 2021.

[23] Castillo, P., Gross, A., Miller, N., Lynch, K. P., and Guildenbecher, D., "Numerical Investigation of Wall-Cooling Effect on Aero-Optical Distortions for Hypersonic Boundary Layer," *AIAA Journal*, Vol. 61, No. 5, 2023, pp. 1911–1924.

[24] Nicoud, F. and Ducros, F., "Subgrid-Scale Stress Modelling Based on the Square of the Velocity Gradient Tensor," *Flow, Turbulence and Combustion*, Vol. 62, No. 3, 1999, pp. 183–200.

[25] Larsson, J., Kawai, S., Bodart, J., and Bermejo-Moreno, I., "Large Eddy Simulation with Modeled Wall-Stress: Recent Progress and Future Directions," *Mechanical Engineering Reviews*, Vol. 3, No. 1, 2015.

[26] Gross, A. and Fasel, H. F., "Multi-block Poisson grid generator for cascade simulations," *Mathematics and Computers in Simulation*, Vol. 79, No. 3, 2008, pp. 416–428.

[27] Gladstone, J. and Dale, T., "Researches on the Refraction, Dispersion, and Sensitivities of Liquids," *Philosophical Transactions of the Royal Society of London*, Vol. 153, 1863, pp. 317–343.

[28] Peck, E., , and Khanna, B., "Dispersion of Nitrogen," *Journal of the Optical Society of America*, Vol. 56, No. 8, 1966.

[29] Clergent, Y., Durou, C., and Laurens, M., "Refractive Index Variations for Argon, Nitrogen and Carbon Dioxide at $\lambda = 632.8$nm (He-Ne Laser Light) in the Range $288.15 \leq \mathrm{T} \leq 323.15$ K, $0 < \mathrm{p} < 110$ kPa," *Journal of Chemical & Engineering Data*, Vol. 44, 1999, pp. 197–199.

[30] Taira, K., Brunton, S. L., Dawson, S. T., Rowley, C. W., Colonius, T., McKeon, B. J., Schmidt, O. T., Gordeyev, S., Theofilis, V., and Ukeiley, L. S., "Modal analysis of fluid flows: An overview," *AIAA Journal*, Vol. 55, No. 12, 2017, pp. 4013–4041.

[31] Lee, S. and Gross, A., "Large-Eddy Simulations of Supersonic Turbulent Boundary Layer," *AIAA Paper 2020-3076*, 2020.

[32] Fassler, A., Leonov, S., and Gordeyev, S., "Optical effects of a temperature-mismatched supersonic mixing layer," *Unconventional Imaging, Sensing, and Adaptive Optics 2023*, Vol. 12693, SPIE, 2023, pp. 383–396.

[33] Sontag, J. and Gordeyev, S., "Optical Diagnostics of Spanwise-Uniform Flows," *AIAA Journal*, Vol. 60, No. 9, 2022, pp. 5031–5045.

[34] Lynch, K., Miller, N., Guildenbecher, D., Butler, L., and Gordeyev, S., "Aero-Optical Measurements of a Mach 8 Boundary Layer," *AIAA Journal*, Vol. 61, No. 3, 2023, pp. 991–1001.

[35] Jumper, E. and Gordeyev, S., "Physics and Measurement of Aero-Optical Effects: Past and Present," *Annual Review of Fluid Mechanics*, Vol. 49, No. 1, 2017, pp. 419–441.

[36] Gordeyev, S. and Juliano, T., "Optical Characterization of Nozzle-Wall Mach-6 Boundary Layers," *AIAA Paper 2016-1586*, 2016.

[37] Miller, N., Lynch, K., Gordeyev, S., Guildenbecher, R., Duan, L., and Wagnild, R., "Aero-optical Distortions of Turbulent Boundary Layers: Hypersonic DNS," *AIAA Paper 2022-0056*, 2022.

[38] Castillo, P., Gross, A., Miller, N., Guildenbecher, D., and Lynch, K., "Wall-Modeled Large-Eddy Simulations of Turbulent Mach 3.5, 8, and 14 Boundary Layers - Effect of Mach Number on Aero-Optical Distortions," *AIAA Paper 2022-3441*, 2022.

[39] Hunt, J. C., Wray, A. A., and Moin, P., "Eddies, streams, and convergence zones in turbulent flows," *Studying turbulence using numerical simulation databases, 2. Proceedings of the 1988 summer program*, 1988.

[40] Fassler, A., Leonov, S., and Gordeyev, S., "Optical Effects of a Temperature-Mismatched and Species-Mismatched Supersonic Mixing Layer," *to be presented at SciTech 2024*, 2024.

[41] Brown, G. L. and Roshko, A., "On density effects and large structure in turbulent mixing layers," *Journal of Fluid Mechanics*, Vol. 64, No. 4, 1974, pp. 775–816.